How brain reacts to attack at a local region

Wenyu Tu[1], Zilu Ma[2], Yuncong Ma[2] and Nanyin Zhang[1,2]*

[1] Neuroscience Program, The Huck Institutes of the Life Sciences, The Pennsylvania State University, University Park, PA 16802, USA

[2] Department of Biomedical Engineering, The Pennsylvania State University, University Park, PA 16802, USA

***Address for correspondence:**

Nanyin Zhang, PhD

Professor of Biomedical Engineering and Electrical Engineering

Lloyd & Dorothy Foehr Huck Chair in Brain Imaging

The Huck Institutes of the Life Sciences

The Pennsylvania State University

W-341 Millennium Science Complex, University Park, PA 16802, USA

Email: nuz2@psu.edu

Conflict of interest: none.

Keywords: DREADD, resting-state fMRI, default mode network, graph theory, awake, rat

Abstract

The brain function is a network phenomenon. The architecture of brain networks has been extensively studied in multiple species. However, exactly how the brain network reconfigures when a local brain region stops functioning is virtually unknown. By combining chemogenetic and resting-state functional magnetic resonance imaging (rsfMRI) methods in an awake rodent model, we investigated the causal impact of inactivating a hub region (i.e. dorsal anterior cingulate cortex) on brain network properties. We found that disrupting hub activity profoundly changed the function and organization of the default-mode network (DMN), as well as DMN-related behavior (i.e. quiet restfulness). It also altered the topological architecture of the whole-brain network in network resilience, segregation and small worldness, but not network integration. These data provide direct evidence supporting the hypothesis that acute dysfunction of a brain hub can cause large-scale network changes. They also comprehensively document the differential impact of inactivating a hub versus a non-hub on network dynamics.

Introduction

The mammalian brain is a highly inter-connected network system with distributed brain regions orchestrating to support normal function and mediate complex behavior (Bullmore and Bassett, 2011). The brain network is organized to maintain an optimal balance of information segregation and integration, which simultaneously maximizes the efficiency of distal communication via long-range connections and minimizes the wiring cost through clustered local processing (Bullmore and Sporns, 2009, 2012). Such organization is well conserved in multiple species including rodents, primates and humans (Liang et al., 2011; Vincent et al., 2007; Wang et al., 2010).

It is becoming increasingly clear that altered brain network organization is tightly linked to brain disorders (Bassett and Bullmore, 2009; Fornito et al., 2015; Liu et al., 2008). However, the neural substrates causing these large-scale network changes remain unknown. A key hypothesis is the dysfunction of brain hub regions. Hubs are brain regions that have high degrees of connections with the rest of the brain (Rubinov and Sporns, 2010; van den Heuvel and Sporns, 2013). Because of their central roles, dysfunction of hub nodes can change global integrative process, and has been hypothesized to be a direct cause of altered brain network properties and pathophysiology of brain disorders (Alstott et al., 2009; Crossley et al., 2014). For instance, brain network analysis in patients with Alzheimer's Disease showed that amyloid-beta deposition mainly accumulated in functional hubs (Buckner et al., 2009). Therefore, comprehensively understanding the causal relationship between hub activity and brain network organization is critical. However, directly testing this hypothesis in humans is challenging, as selectively altering activity in a hub and dissecting its causal impact on brain networks are difficult.

This obstacle can be overcome in experimental animals using neuroscience tools like Designer Receptors Exclusively Activated by Designer Drugs (DREADDs) and resting state functional magnetic resonance imaging (rsfMRI). DREADDs introduce genetically encoded modified muscarinic G-protein-coupled receptors into living neurons, which allow reversible *in vivo* manipulation of neuronal activity of a defined brain region for hours (Armbruster et al., 2007). rsfMRI measures brain-wide resting-state functional connectivity (RSFC), and provides comprehensive assessment of brain network properties (Biswal et al., 1995; Liang et al., 2011). Thus, combining these two techniques offers a system that allows us to characterize the reconfiguration of the brain network as the neural activity of a network node is selectively perturbed. In addition, given the highly conserved brain network architecture in the mammalian brain (Liang et al., 2011; Vincent et al., 2007; Wang et al., 2010), the results are translatable to humans.

Here we investigate the causal impact of manipulating a hub region, dorsal anterior cingulate cortex (dACC), on brain network function and organization, as well as behavior using an awake rodent model established in our lab (Dopfel et al., 2019; Ma et al., 2018; Ma and Zhang, 2018; Zhang et al., 2010). Imaging awake rodents avoids the confounding effects of anesthesia (Gao et al., 2016; Hamilton et al., 2017; Liang et al., 2012b; Ma et al., 2017), and permits linking imaging and behavioral data (Dopfel et al., 2019; Liang et al., 2014). dACC is selected because it is a known functional and anatomical hub in both human and rat brain (Ma et al., 2018; van den Heuvel et al., 2016; van den Heuvel and Sporns, 2013), (Bush et al., 2000). We first examine the impact of suppressing the dACC on the default mode network (DMN), which is composed of a group of distributed brain regions exhibiting higher activity at rest (Gusnard et al., 2001; Raichle et al., 2001). DMN

83 function is tightly linked to self-referential mental activity in humans, and its abnormality
84 has been linked to numerous brain disorders (Whitfield-Gabrieli and Ford, 2012; Zhang
85 and Raichle, 2010). DMN has also been reported in rodents and primates (Hsu et al.,
86 2016; Lu et al., 2012; Stafford et al., 2014; Vincent et al., 2007; Zhou et al., 2016),
87 although our understanding of DMN in animals is mostly limited to its anatomical
88 resemblance to the DMN in humans (Lu et al., 2012; Vincent et al., 2007). Since dACC
89 is a hub node in the rodent DMN (Hsu et al., 2016), manipulating dACC activity provides
90 an avenue for understanding the rodent DMN at the functional level. Our data show that
91 suppressing the dACC disrupts activity and connectivity across the whole DMN, and
92 changes DMN-related behaviors. These data suggest that, like humans, DMN in rodents
93 is a functional network with coordinated activity to mediate behavior. Furthermore, we
94 demonstrate that suppressing the dACC impacts the organization of the whole-brain
95 network including network resilience, segregation and small worldness, but not network
96 integration. All these changes are absent in sham rats or when a non-hub region is
97 suppressed. Taken together, this study provides direct measurement of the brain's
98 response to local attack, and presents a comprehensive framework demonstrating the
99 pivotal role of hubs in the brain network.
100

101 ## Results

102 Animals were stereotactically injected with adeno-associated viruses (AAVs)
103 expressing inhibitory G-protein coupled hM4Di receptor with a pan-neuronal synapsin
104 promoter (AAV8.hSyn.hM4Di.mCherry, Addgene). After 4-6 weeks of recovery and
105 protein expression (Fig. S1), animals received either Clozapine-N-Oxide (CNO) or saline

106 30 min before electrophysiology recording, rsfMRI scanning or behavioral tests. Saline
107 and CNO sessions were separated by at least 3 days in a random order. The experimental
108 procedure is summarized in Fig. 1.
109
110 *DREADD suppressed both evoked and spontaneous neural activities in the injected site.*
111 We first validated the inhibitory effect of the DREADD using a visual stimulation
112 paradigm (Fig.2). AAVs expressing inhibitory DREADD (AAV8.hSyn.hM4Di.mCherry,
113 Addgene) were injected into the superior colliculus (SC). After recovery and DREADD
114 expression, neural activity in the SC was activated by visual stimuli (Figs. 2A-D, 1
115 flash/trial and 5 flashes/trial, 100ms per flash, 10 sec per trial, 15 trials per animal) and
116 measured by electrophysiology. SC firing rates were significantly reduced 30 min after
117 CNO injection (1 flash/trial: two-sample tests, $t = 10.30$, $p = 8.8 \times 10^{-17}$, Figs. 2B & D; 5
118 flash/trial, $t = 13.48$, $p = 4.1 \times 10^{-23}$, Fig. 2C & D). In addition, spontaneous neural activities
119 including spiking activity and local field potential (LFP), quantified by the
120 electrophysiology data 5s before the onset of visual stimulation in each trial, were
121 significantly dampened in CNO-injected rats (MUA: $t = 16.15$, $p = 1.041 \times 10^{-36}$; LFP: $t =$
122 5.84, $p = 8.6 \times 10^{-8}$; Figs. 2E, F & G). The LFP spectrograms after saline and CNO
123 injections in a representative rat were also shown in Fig. S2. These data collectively
124 confirmed the inhibitory effect of the DREADD on evoked and spontaneous neural
125 activities in rats.
126
127 *Suppressing the dACC reduced its rsfMRI signal, RSFC and local network organization.*
128 The bilateral dACC was transfected by inhibitory DREADDs under a pan-neuronal

129 synapsin promoter (AAV8.hSyn.hM4Di.mCherry, Addgene). Sham rats received a control
130 virus (AAV8-hsy-GFP, Addgene). Animals were scanned using rsfMRI twice in the awake
131 state, with each session starting 30 min after either CNO or saline injections. The two
132 imaging sessions were separated by at least 3 days with a randomized order. There was
133 no difference in motion level during rsfMRI scanning between CNO and saline injection
134 conditions in both DREADD and sham groups (Fig. S3).

135 Fig. 3A shows that DREADD suppression of the dACC reduced its resting-state
136 blood-oxygenation-level dependent (BOLD) amplitude (std divided by mean, $t = 2.00$, $p =$
137 0.048), again confirming the inhibitory effect of the DREADD on spontaneous neural
138 activity. Suppressing the dACC also affected its functional connectivity, reflected by
139 generally reduced RSFC in the dACC seedmaps (one sample t test, $p<0.0005$, linear
140 mixed model, false discovery rate (FDR) corrected) after CNO injection relative to saline
141 injection (Fig. 3B). We further examined the impact of suppressing the dACC on its local
142 information processing, assessed using the modular structure, which is defined as a
143 group of nodes with significantly greater within-module connections than between-module
144 connections (Newman, 2006). The dACC-related module shrunk in size in DREADD rats
145 after CNO injection relative to saline injection at high graph densities ($p < 0.05$, linear
146 mixed model, Fig. 3E), suggesting that suppressing the dACC mainly dropped relatively
147 weaker connections in the dACC module.

148 In addition to dACC-related circuits, RSFC in distributed connections was altered
149 (two-sample t-tests, $p < 0.05$, linear mixed model, FDR corrected) with lower RSFC in the
150 majority of these connections (i.e. blue elements in the T map, Figs. 3C & 3D), indicating
151 that the impact of suppressing neural activity in a hub can go beyond the hub itself and

propagate to neural circuits across the whole brain. This ripple effect is consistent with the report in human patients with focal brain lesions to critical locations (Gratton et al., 2012).

None of these changes (i.e. resting-state BOLD amplitude, dACC-related RSFC and community size) were observed in sham rats when comparing CNO- to saline-injection conditions (Fig. S4), which suggests that CNO had minimal off-target effects in our system, ruling out its potential confounding effects on rsfMRI data (Gomez et al., 2017).

Suppressing dACC altered activity and connectivity in the DMN.

Given that dACC is a major hub node in the functional network of DMN, we examined the impact of inactivating the dACC on the DMN organization in awake rodents. We first constructed the DMN using *fractional amplitude of low-frequency fluctuations* (fALFF), defined by voxel-wise low-frequency spectrum power (0.01–0.08 Hz) normalized by the full-spectrum power (Zou et al., 2008) of the rsfMRI signal. This well-established method measures the amplitude of regional spontaneous brain activity. As a result, it can reliably identify brain regions with higher activity at rest, and map the spatial pattern of the DMN (Zou et al., 2008).

Fig. 4 displays the DMN spatial maps in DREADD and sham rats after saline and CNO injections, respectively. Brain regions highlighted in the network included the ACC, posterior cingulate cortex (PCC), prelimbic cortex (PL), retrosplenial cortex (RSC), orbital cortex (ORB), posterior parietal cortex (PPC), as well as subcortical regions of the basal forebrain (BF) and hypothalamus (Hypo). This DMN pattern was reproduced with a

175 completely different method (i.e. independent component analysis, Fig. S5) previously
176 used by other groups, and well agreed with the rodent DMN pattern reported in the
177 literature (Hsu et al., 2016; Lu et al., 2012; Stafford et al., 2014). Notably, we found that
178 the BF was a prominent node in the rodent DMN, which was not observed in other rodent
179 DMN mapping studies, but was reported in an electrophysiology study that demonstrated
180 that the BF is a key DMN node and critical in regulating DMN-related behaviors in rats
181 (Nair et al., 2018).

182 Intriguingly, suppressing one node in the DMN (i.e. dACC) dampened the activity
183 of virtually the entire network (Fig. 4A, top row), reflected by reduced BOLD fALFF in the
184 ACC, PL, ORB, PPC, BF and Hypo after CNO injection in DREADD-suppressed rats (Fig.
185 4B, two row, $p < 0.05$, Family-wise error corrected). Again, no regions displayed reduced
186 spontaneous activity in sham rats after CNO injection (Figs. 4A & 4B, bottom row). We
187 also calculated RSFC between every pair of nodes in the DMN including the dorsal and
188 ventral ACC, dorsal and ventral PCC, RSC, ORB, PL, PPC, as well as BF and Hypo (Hsu
189 et al., 2016) in both DREADD and sham rats after saline and CNO injections, respectively
190 (Fig. 4C). Cortical nodes generally displayed significantly reduced RSFC ($p < 0.05$, FDR
191 corrected, Figs. 4D & 4E), except that the RSC exhibited increased RSFC with the PPC,
192 BF and Hypo. This result is consistent with our observation that RSC emerged as a new
193 hub in the whole-brain network when the dACC was suppressed (Fig. 7). In contrast, both
194 subcortical nodes (BF and Hypo) showed increased RSFC after dACC suppression (Figs.
195 4D & 4E). Taken together, these data revealed that the DMN was significantly
196 reorganized when dACC activity was suppressed, suggesting that the rodent DMN is a
197 functional network with coordinated activity, and the dACC is a pivotal node in this network.

198

199 *Suppressing dACC altered DMN-related behaviors in animals.*

200 Considering that suppressing dACC significantly altered DMN activity in awake
201 rodents, we hypothesize that it also changes DMN-related behavior, measured by quiet
202 restfulness in rodents. Nair and colleagues demonstrated that quiet restfulness in home-
203 cage is characteristic behavior to DMN activity, evidenced by elevated neural activity in
204 the DMN, including ACC and BF, during this behavioral state (Nair et al., 2018). Robust
205 DMN activation during quiet restfulness was also reported in chimpanzees (Barks et al.,
206 2015). Therefore, we evaluated quiet restfulness, defined by continuous immobility for at
207 least 2s, in our animals. After either CNO or saline injection, the rat was put in the home
208 cage for 45min and was video-recorded. The animal's behavior was analyzed using
209 behavioral tracking software (ANY-maze, Stoelting Co., Wood Dale, IL). After CNO
210 injection, quiet restfulness was significantly reduced in the rat (Fig. 5), reflected by
211 significantly lower immobile time for at least 2s ($t = 3.991$, $p = 0.0009$), but higher distance
212 travelled ($t = 4.294$, $p = 0.0004$), mean speed ($t = 4.811$, $p = 0.0001$) and total mobile time
213 ($t = 3.991$, $p = 0.0009$). Rats also displayed significantly higher rearing after CNO injection
214 ($t = 2.80$, $p = 0.01$), likely reflecting an increase in vigilance and/or exploratory behavior.
215 Reduced quiet restfulness remained consistent during the last 15 min of testing,
216 suggesting that these behavioral changes were not due to the environmental changes at
217 the beginning of the test (Fig. S6). These data demonstrate that dACC suppression
218 reduced DMN-related behaviors in rats, echoing their dampened DMN activity.

219

220 *Suppressing a hub node changed whole-brain network organization*

221 We further investigated the effect of suppressing the dACC on the organization of
222 the whole-brain network architecture in four aspects: network resilience, functional
223 segregation, functional integration, and small-worldness. The whole rat brain was
224 parcellated into 68 bilateral regions of interest (ROIs) based on the Swanson atlas
225 (Swanson, 2004). The whole-brain network was constructed by calculating RSFC
226 between every two ROIs, generating a RSFC matrix for each animal at each condition.
227 This RSFC matrix was then binarized based on graph density. Graph topological
228 parameters including assortativity, modularity, global efficiency, and small-worldness
229 were respectively calculated as a function of graph density.

230 Assortativity measures network resilience. Brain networks with high assortativity
231 are more resistant to local attack such as lesion and neurological degeneration (Newman,
232 2002; Rubinov and Sporns, 2010). Fig. 6 shows that suppressing the dACC considerably
233 reduced the network assortativity, and as a consequence, the whole-brain network
234 became more vulnerable (Fig. 6A). Functional segregation, quantified by modularity,
235 measures the network's ability of specialized processing. We observed that dACC
236 suppression decreased the modularity of the global brain network, indicating reduced
237 functional segregation (Fig. 6C). Global efficiency measures functional integration, which
238 assesses the ability to integrate specialized information from distributed brain regions.
239 Interestingly, suppressing the dACC did not seem to affect the global efficiency (Fig. 6D).
240 Small-worldness reflects the ability to balance functional segregation and integration.
241 Suppressing the dACC reduced small-worldness of the whole-brain network (Fig. 6B). In
242 summary, we observed that suppression of the dACC affected global brain topology
243 including network resilience, network segregation and small-worldness, but not network

integration.

As expected, DREADD suppression of the dACC significantly lowered its degree (Fig. 7), suggesting that dACC lost its hubness in the network. Interestingly, the degree of the ventral RSC was significantly increased after dACC suppression, consistent with our data that some RSC connections increased their RSFC within the DMN (Fig. 4D). Again, no changes in the degree of dACC or RSC were observed in sham rats (Fig. S7). These results indicate that a new hub can emerge when an existing hub stops functioning, likely due to the compensatory mechanism.

Suppression of a non-hub region did not change whole-brain network properties

To determine whether aforementioned network changes depended on the specific role of the node (i.e. hub versus non-hub), we also suppressed the activity in a non-hub region—primary visual cortex (V1, bilateral) (Ma et al., 2018) using the same pan-neuronal inhibitory DREADD. After CNO injection, significantly reduced BOLD amplitude in V1 was observed (Fig. 8A), which confirmed the inhibitory effect of DREADD in V1. However, suppression of V1 did not affect fALFF in the DMN (Fig. S8), nor did it cause any whole-brain topological changes including network resilience, functional segregation, functional integration, or small-worldness (Figs. 8B-8E). Taken together, these data suggest that attack on separate brain regions can have differential impact on brain network properties, and hub nodes are particularly vulnerable to such attacks.

Discussion

For over a century, the neuroscience field has been tremendously moved forward

267 by the effort of examining the relationship between damage of specific brain regions and
268 loss of certain brain function. Classical examples are the discovery of the inferior frontal
269 gyrus in speech production by Paul Broca, and the left posterior temporal cortex in
270 language comprehension by Carl Wernicke. Despite this vital advancement, converging
271 evidence suggests that a large number of complex tasks involve numerous cognitive
272 processes and require integrated activity from multiple brain regions (Liegeois et al.,
273 2019). Therefore, brain function should be viewed as a network phenomenon.

274 By combining DREADDs and rsfMRI in an awake rodent model, we established a
275 system that allowed us to manipulate the activity in any brain region, and measure the
276 corresponding changes in brain-wide networks. This system makes it possible to
277 mechanistically dissect the causal relationship between a (or multiple) local brain region(s)
278 and brain network properties. In this study we specifically investigated the role of a hub
279 region (i.e. dACC) in brain networks. We found that disrupting hub activity profoundly
280 changed the function and organization of the DMN (Figs 4), as well as DMN-related
281 behavior (Fig. 5). It also altered the topological architecture of the whole-brain network in
282 terms of network resilience, segregation and small worldness, but not network integration
283 (Fig. 6). These data offer direct evidence supporting the hypothesis that acute dysfunction
284 of a brain hub can cause large-scale network and behavioral changes. They also provide
285 a comprehensive framework documenting the differential impact of inactivating a hub
286 versus a non-hub node on network dynamics.

287

288 *Tight relationship between local regions and brain networks*

289 The activity in local brain regions can be manipulated using tools like

290 chemogenetic, optogenetic, pharmacological and lesion methods. Such perturbations are
291 often used to study the role of a specific brain region in behavior (Whissell et al., 2016).
292 Meanwhile, the capacity of manipulating local brain regions can be tremendously
293 expanded when combined with neuroimaging approaches with a global field of view (e.g.
294 fMRI), as the causal impact of local region dysfunction on the rest of the interconnected
295 network can be monitored across the whole brain (Lee et al., 2010). For instance, using
296 DREADDs and rsfMRI, Grayson and colleagues showed that inactivating the amygdala
297 disrupted communication throughout the cortex and altered the topology of the global
298 brain network in anesthetized monkeys (Grayson et al., 2016). This observation echoes
299 human patient studies in which lesions of critical focal brain locations caused widespread
300 disruption of the brain modular structure and behavior (Gratton et al., 2012; Warren et al.,
301 2014). These results collectively suggest tight links among regional activity, large-scale
302 network properties and behavior, and highlight the importance of combining local
303 perturbations and global network measurement. Uniquely, our study was conducted in
304 awake animals, which avoids the confounding effects of anesthesia on brain network
305 function, and permits direct association of network features and behavioral changes
306 resulting from hub inactivation. This nature also makes the findings translatable to
307 humans, considering numerous reports of large-scale brain network changes in human
308 brain disorders.
309
310 *DREADDs vs lesion*
311 There are several advantages choosing the DREADD over the lesion method for
312 our research purpose. First, DREADDs allow us to specifically and reversibly inhibit a

313 brain region with minimal damage. On the other hand, long-term damage in brain tissue
314 can decrease metabolism and alter local vascular structure. In addition, there can be
315 excessive blood flow in surrounding regions (Rorden and Karnath, 2004). All these factors
316 will impact fMRI data measurement and can confound RSFC results. Long-term lesion
317 studies can also be compounded by post-lesion neural plasticity changes resulting from
318 the compensatory mechanism (i.e. secondary effects). Furthermore, most psychiatric
319 disorders are linked to loss of function without tissue damage, making the DREADD
320 method a better translatable model.
321
322 *DMN in rodents – beyond anatomical resemblance with other species*
323 We observed significant reconfiguration of the DMN after transiently inactivating
324 one of its hub nodes (i.e. dACC) in awake rodents. This finding was corroborated by
325 altered DMN-related behaviors after dACC suppression. Although the DMN has been
326 extensively studied in humans including its network structure, function and clinical
327 implications, our understanding of the DMN in rodents is limited. The discovery of rodent
328 DMN was mainly based on the anatomical resemblance of the network structure with the
329 DMN in humans and primates (Lu et al., 2012; Stafford et al., 2014), but its functional role
330 in behavior remains unclear. Nair and colleagues showed that the rat BF exhibited
331 pronounced gamma oscillations during DMN-related behaviors and this activity was
332 suppressed during active exploration of an unfamiliar environment (Nair et al., 2018),
333 suggesting that the BF might be a key DMN node that regulates DMN activity. They further
334 demonstrated that the BF controls DMN-related behaviors by affecting neural activity in
335 the ACC. These results are in remarkable consistency with our findings. First, we also

336 observed prominent involvement of the BF in the rat DMN at baseline, which was missing
337 in previous rodent DMN mapping studies (Hsu et al., 2016; Lu et al., 2012). Notably, the
338 BF has strong connections with the cortex and subcortical regions like Hypo, and these
339 connected regions substantially overlapped with the DMN revealed in our study
340 (Agostinelli et al., 2019; Gielow and Zaborszky, 2017). Second, suppressing the dACC
341 considerably dampened the DMN activity, including that involving the BF. Third,
342 suppressing dACC reduced DMN-related behaviors. Taken together, these results
343 support the concept that, like humans and primates, the DMN in rodents is a functional
344 network with coordinated neural activity from distributed brain regions, and this network
345 might support behavior related to internally oriented brain states.
346
347 *Hubs and brain network topology*
348 The topological changes resulting from hub inactivation, including reduced network
349 resilience, segregation and small worldness, are important for our understanding of the
350 role of individual regions in the global brain network organization. A brain network can be
351 modeled as a graph composed of spatially distributed neuronal components as nodes
352 and anatomical or functional associations between components as edges (Bullmore and
353 Sporns, 2009, 2012). Topological features of the brain graph are critical in understanding
354 inter-areal information exchange in health and disease. Although the architecture of brain
355 networks has been extensively studied in multiple species (Bassett and Bullmore, 2006;
356 Belcher et al., 2013; Liang et al., 2011; Liska et al., 2015), it remains elusive whether
357 different types of nodes, such as hubs versus non-hubs, play distinct or similar roles in
358 the topology of the global brain network. Our data revealed that changes in a hub, but not

359 a non-hub, can significantly alter brain network topology. These results provide critical
360 insight into understanding the pathogenesis of neurological and psychiatric disorders,
361 which indicate that altered brain topological properties reported in these brain disorders
362 might start from dysfunction of certain hub nodes (Seeley et al., 2009). Interestingly, our
363 data showed that network integration was intact after dACC inactivation, likely due to the
364 compensatory effect of the so-called 'rich club organization' in the rat brain (Ma et al.,
365 2018). Another possible explanation is that although the dACC has high centrality, it
366 functions as a provincial hub as opposed to a connector hub (Guimera and Nunes Amaral,
367 2005). These two types of hubs were demonstrated to have differential impact on brain
368 network properties (Gratton et al., 2012), with connector hubs more affecting network
369 integration, and provincial hubs more affecting network segregation. Our result is
370 consistent with the notion that the ACC belongs to the "segregation effect" class, which
371 agrees with the report in human lesion studies (Yuan et al., 2017).
372

373 **Methods and Materials**

374 *Animals.*

375 44 adult male Long-Evans rats (300-500g) were used in the present study. Animals
376 were housed in Plexiglas cages. Food and water were provided *ad libitum*. The housing
377 room was maintained at an ambient temperature (22-24 ˚C) with a 12h light:12h dark
378 cycle. All experiments were approved by the Pennsylvania State University Institutional
379 Animal Care and Use Committee.
380

381 *Surgery.*

382 Aseptic stereotaxic surgery was conducted to infuse the virus to the brain. Rats
383 were anesthetized by intramuscular (IM) injections of ketamine (40 mg/kg) and xylazine
384 (12 mg/kg). Dexamethasone (0.5 mg/kg) and Baytril (2.5 mg/kg) were injected SQ to
385 prevent tissue inflammation and bacterial infections. During the surgery, respiration was
386 controlled by a ventilator with artificial oxygen. The heart rate was monitored by a pulse
387 oximetry (MouseSTAT® Jr., Kent Scientific Corporation), and the body temperature was
388 maintained at 37 ˚C with a warming pad (PhysioSuite, Kent Scientific Corporation). The
389 DREADD virus (AAV8-hSyn-hM4Di-mCherry, 1 μL at titer ≥ 3×10^{12} vg/mL, Addgene,
390 Watertown, MA) was bilaterally injected into the dACC (coordinates: AP +2, ML +/-0.5,
391 DV -1) and the primary visual cortex (coordinates: AP -6.5, ML +/-3.5, DV -1) for the hub
392 (n = 25) and non-hub (n = 8) groups, respectively [24]. Sham rats were injected with a
393 control virus (AAV8-hsy-GFP, 1 μL at titer ≥ 3×10^{12} vg/mL, Addgene, Watertown, MA, n
394 = 8)[24] into the dACC. In addition, separate animals used in the visual stimulation
395 experiment were unilaterally injected with AAV8-hSyn-hM4Di-mCherry (1 μL at titer ≥
396 3×10^{12} vg/mL, Addgene, Watertown, MA, n = 3) in the SC (coordinates: AP -7, ML +1.5,
397 DV -3). Rats were allowed to recover for at least four weeks.
398
399 *fMRI experiments:*
400 Before imaging, animals were acclimated to the MRI environment for 7 days in
401 order to minimize stress and motion during imaging. To better adapt the animal to the
402 restrainer and scanning environment, the acclimation period was gradually increased
403 from 15 min on Day 1 to 30 min on Day 2, 45 min on Day 3, and maintained at 60 min/day
404 for Days 4-7. Detailed procedures for acclimation can be found from our previous

405 publications (Dopfel and Zhang, 2018; Liang et al., 2012a). A similar approach to imaging
406 awake animals has also been adopted by other research groups in multiple species
407 (Bergmann et al., 2016; Chang et al., 2016; Yoshida et al., 2016). CNO (1mg/kg in saline,
408 dissolved in DMSO, Sigma-Aldrich, St. Louis, MO) or saline (with DMSO) was IP injected
409 30 min before rsfMRI data acquisition, at a random order with at least three days apart.

410 All imaging sections were conducted at the High Field MRI Facility at the
411 Pennsylvania State University on a 7T Bruker 70/30 BioSpec running ParaVision 6.0.1
412 (Bruker, Billerica, MA). rsfMRI data were acquired at the awake state using T2*-weighted
413 gradient-echo rsfMRI images using the echo-planar-imaging (EPI) sequence with the
414 following parameters: repetition time = 1000ms; echo time = 15ms; matrix size = 64×64;
415 field of view = 3.2 × 3.2 cm^2; slice number = 20; slice thickness = 1mm; flip angle = 60;
416 600 volume each run. Three runs were acquired each rsfMRI session. Raw EPI images
417 were shown in Fig. S9.

418

419 *Data analysis:*

420 All acquired image data were aligned to a defined atlas using Medical Image
421 Visualization and Analysis software (MIVA, http://ccni.wpi.edu/), and then subjected to
422 motion correlation (SPM12), spatial smoothing (Gaussian kernel, full-width at half-
423 maximum = 1 mm), voxel-wise nuisance regression of motion parameters, as well as the
424 signals from the white matter and ventricles, and bandpass filtering (0.01-0.1Hz). Before
425 these steps, rsfMRI volumes with relative framewise displacement (FD) > 0.25 mm and
426 the preceding and following volumes were removed. In addition, the first 10 volumes of
427 each rsfMRI scan were discarded to ensure steady state of magnetization. rsfMRI scans

428 with > 15% volumes discarded were removed from further analysis.

429 fALFF was determined by calculating the ratio of the power in the low-frequency
430 range (0.01–0.08 Hz) to that of the full spectrum (0–0.25 Hz). For each voxel, the time
431 course was detrended without a band-pass filtering, and then transformed to the
432 frequency domain using FFT. We calculated the ratio between the square root of power
433 in the range of 0.01–0.08 Hz and that across the entire frequency range. fALFF changes
434 after DREADD inhibition were obtained using voxel-wise two-sample t-tests with family
435 wise error correction (P<0.05, FWE corrected) between data acquired after CNO injection
436 versus saline injection.

437 Seed RSFC maps were generated using seed-based correlation analysis. Pearson
438 cross-correlation coefficients between the regionally averaged time course from all voxels
439 inside the seed and time courses of individual voxels were calculated. The corresponding
440 correlation coefficients were Fisher transformed, averaged across all scans and animals
441 in each group, and transformed back to r values.

442 The whole-brain RSFC network was constructed by parcellating the rat brain into
443 68 anatomical ROIs based on the Swanson Atlas (Swanson, 2004), which were also
444 grouped into 10 functional systems including amygdala complex, striatum, hypothalamus,
445 hippocampus, thalamus, sensory-motor cortex, polymodal association cortex, brainstem,
446 pallidum, and retro-hippocampal regions. RSFC between each pair of ROIs was
447 calculated by Pearson correlation of regionally averaged time series of the ROIs.

448 A hub score of each node ranged from 0-4 was determined by the number of the
449 following four criteria the node met: (1) 20% highest degree; (2) 20% highest
450 betweenness centrality; (3) 20% lowest characteristic path length; (4) 20% lowest local

clustering coefficient.

Topological parameters of the whole-brain network including the modularity, global efficiency, small-worldness, and assortativity were calculated on binarized network across the graph density ranging from 0.15 to 0.45 with a step of 0.05 using the brain connectivity toolbox (BCT) [30] based on the following equations:

Assortativity (Newman, 2002):

$$r = \frac{l^{-1}\sum_{(x,y\in L)} k_x k_y - \left[l^{-1}\sum_{(x,y\in L)} \frac{1}{2}(k_x + k_y)\right]^2}{l^{-1}\sum_{(x,y\in L)} \frac{1}{2}(k_x^2 + k_y^2) - \left[l^{-1}\sum_{(x,y\in L)} \frac{1}{2}(k_x + k_y)\right]^2}$$

where $\mathrm{k_x}, \mathrm{k_y}$ is the degree of node x and y on two opposite ends of an edge; L is the set of all edges within the network, and l is total number of edges.

Modularity (Newman, 2004):

$$Q = \sum_{i\in M}[e_{ii} - (\sum_{j\in M} e_{ij})^2]$$

where M represents a set of non-overlapping modules, and $\mathrm{e_{ij}}$ is the proportion of between-modules connections of module i and j; $\mathrm{e_{ii}}$ is the proportion of within-modules connections of module i.

Global efficiency (Latora and Marchiori, 2001):

$$E = \frac{1}{n}\sum_{i\in N}\frac{\sum_{y\in N, y\neq x} d_{xy}^{-1}}{n-1}$$

where n is the total number of nodes; N is the set of all nodes. d_{xy} is the shortest path length between nodes x and y,

Small-worldness (Humphries and Gurney, 2008):

472 $$S = \frac{C/C_{rand}}{L/L_{rand}}$$

473 where C and C_{rand} are the clustering coefficients of the testing network and a random
474 network, respectively; L and L_{rand} are the characteristic path lengths of the testing
475 network and a random network.

476 At each graph density, all topological parameters were determined for each scan.
477 Changes in each parameter was determined by two-sample t-tests (linear mixed model)
478 between the CNO injection and saline injection conditions.

479

480 *Behavioral Test*

481 Animals underwent two behavioral sessions with either CNO or saline injection
482 with a random sequence separated by at least 7 days. Each session was composed of a
483 45 min home-cage test. Before the test, the animal was acclimated to the behavioral room
484 for 15 min, followed by either CNO (1mg/kg) or saline injection. The animal was then put
485 back to its home-cage in the behavioral room for 45 min. Behaviors including the total
486 distance traveled, mean speed, time of mobility and time of immobility for at least 2s were
487 recorded by an infrared camera and analyzed by behavioral tracking software (ANY-maze,
488 Stoelting Co., Wood Dale, IL).

489

490 *Electrophysiology*.

491 Electrophysiology recordings were conducted in animals with inhibitory DREADD
492 expressed in the SC. Rats were initially anesthetized by IM injections of ketamine (40
493 mg/kg) and xylazine (12 mg/kg). An electrode (Neuronexus, Ann Arbor, MI) was then
494 inserted into the SC to measure visually-evoked neuronal response to light stimulation

495 produced by a blue laser source (100 mW, 473 nm, Opto Engine) coupled with an optic
496 fiber, which was placed 5 cm away from the contralateral eye. Before recording, rats were
497 injected with either saline or CNO in each session. During recording, light anesthesia was
498 maintained using isoflurane (~0.75%). Each session included 15 trials of visual
499 stimulation, presented as a single light flash (100 ms per flash) or five flashes (100 ms
500 each flash, 100 ms inter-flash interval) every 10 s. Light stimulation was controlled by a
501 custom Labview program. The electrophysiological signal was amplified and sampled at
502 25 kHz using a Neuronexus recording system (Neuronexus, Ann Arbor, MI). Raw data
503 were bandpass filtered (MUA: 300-3000 Hz, LFP: 3-300 Hz). Spikes larger than three
504 times of the standard deviation of electrophysiological signal were detected and clustered
505 at a bin size of 50 ms in peristimulus-timed histograms (PSTHs).
506
507 *Histology.*
508 After electrophysiology, animal was perfused with saline followed by 4% PFA
509 solution. The brain was taken out carefully and stored in solution with 4%
510 paraformaldehyde and 20% sucrose. After fixation, the brain was sliced into 60μm slices.
511 Fluorescent expression in the injection site was examined under microscopy.
512
513 **Acknowledgments**
514 We would like to thank Yikang Liu and David Dopfel for their technical support. The
515 present study was partially supported by National Institute of Neurological Disorders and
516 Stroke Grant R01NS085200 (PI: Nanyin Zhang, PhD) and National Institute of Mental
517 Health Grant R01MH098003 and RF1MH114224 (PI: Nanyin Zhang, PhD).

Author Contributions: N.Z. designed the research; W.T., Z.M. and Y.M. performed animal experiments; W.T. and Y.M. performed data analysis; N.Z. and W.T. wrote the paper.

Conflict of interest: the Authors declare no competing interests.

Data availability: Data supporting the findings of this manuscript are available from the corresponding author upon reasonable request.

References:

Agostinelli, L.J., Geerling, J.C., and Scammell, T.E. (2019). Basal forebrain subcortical projections. Brain structure & function 224, 1097-1117.

Alstott, J., Breakspear, M., Hagmann, P., Cammoun, L., and Sporns, O. (2009). Modeling the impact of lesions in the human brain. PLoS Comput Biol 5, e1000408.

Armbruster, B.N., Li, X., Pausch, M.H., Herlitze, S., and Roth, B.L. (2007). Evolving the lock to fit the key to create a family of G protein-coupled receptors potently activated by an inert ligand. Proc Natl Acad Sci U S A 104, 5163-5168.

Barks, S.K., Parr, L.A., and Rilling, J.K. (2015). The default mode network in chimpanzees (Pan troglodytes) is similar to that of humans. Cereb Cortex 25, 538-544.

Bassett, D.S., and Bullmore, E. (2006). Small-world brain networks. Neuroscientist 12, 512-523.

Bassett, D.S., and Bullmore, E.T. (2009). Human brain networks in health and disease. Curr Opin Neurol 22, 340-347.

Belcher, A.M., Yen, C.C., Stepp, H., Gu, H., Lu, H., Yang, Y., Silva, A.C., and Stein, E.A. (2013). Large-scale brain networks in the awake, truly resting marmoset monkey. J Neurosci 33, 16796-16804.

Bergmann, E., Zur, G., Bershadsky, G., and Kahn, I. (2016). The Organization of Mouse and Human Cortico-Hippocampal Networks Estimated by Intrinsic Functional Connectivity. Cereb Cortex 26, 4497-4512.

Biswal, B., Yetkin, F.Z., Haughton, V.M., and Hyde, J.S. (1995). Functional connectivity in the motor cortex of resting human brain using echo-planar MRI. Magn Reson Med 34, 537-541.

Buckner, R.L., Sepulcre, J., Talukdar, T., Krienen, F.M., Liu, H., Hedden, T., Andrews-Hanna, J.R., Sperling, R.A., and Johnson, K.A. (2009). Cortical hubs revealed by intrinsic functional connectivity: mapping, assessment of stability, and relation to Alzheimer's disease. J Neurosci 29, 1860-1873.

Bullmore, E., and Sporns, O. (2009). Complex brain networks: graph theoretical analysis of structural and functional systems. Nat Rev Neurosci 10, 186-198.

557 Bullmore, E., and Sporns, O. (2012). The economy of brain network organization. Nat
558 Rev Neurosci 13, 336-349.
559 Bullmore, E.T., and Bassett, D.S. (2011). Brain graphs: graphical models of the human
560 brain connectome. Annu Rev Clin Psychol 7, 113-140.
561 Bush, G., Luu, P., and Posner, M.I. (2000). Cognitive and emotional influences in anterior
562 cingulate cortex. Trends Cogn Sci 4, 215-222.
563 Chang, P.C., Procissi, D., Bao, Q., Centeno, M.V., Baria, A., and Apkarian, A.V. (2016).
564 Novel method for functional brain imaging in awake minimally restrained rats. J
565 Neurophysiol 116, 61-80.
566 Crossley, N.A., Mechelli, A., Scott, J., Carletti, F., Fox, P.T., McGuire, P., and Bullmore,
567 E.T. (2014). The hubs of the human connectome are generally implicated in the
568 anatomy of brain disorders. Brain 137, 2382-2395.
569 Dopfel, D., Perez, P.D., Verbitsky, A., Bravo-Rivera, H., Ma, Y., Quirk, G.J., and Zhang,
570 N. (2019). Individual variability in behavior and functional networks predicts
571 vulnerability using an animal model of PTSD. Nat Commun 10, 2372.
572 Dopfel, D., and Zhang, N. (2018). Mapping stress networks using functional magnetic
573 resonance imaging in awake animals. Neurobiol Stress 9, 251-263.
574 Fornito, A., Zalesky, A., and Breakspear, M. (2015). The connectomics of brain disorders.
575 Nat Rev Neurosci 16, 159-172.
576 Gao, Y.R., Ma, Y., Zhang, Q., Winder, A.T., Liang, Z., Antinori, L., Drew, P.J., and Zhang,
577 N. (2016). Time to wake up: Studying neurovascular coupling and brain-wide
578 circuit function in the un-anesthetized animal. Neuroimage.
579 Gielow, M.R., and Zaborszky, L. (2017). The Input-Output Relationship of the Cholinergic
580 Basal Forebrain. Cell Rep 18, 1817-1830.
581 Gomez, J.L., Bonaventura, J., Lesniak, W., Mathews, W.B., Sysa-Shah, P., Rodriguez,
582 L.A., Ellis, R.J., Richie, C.T., Harvey, B.K., Dannals, R.F., *et al.* (2017).
583 Chemogenetics revealed: DREADD occupancy and activation via converted
584 clozapine. Science 357, 503-507.
585 Gratton, C., Nomura, E.M., Perez, F., and D'Esposito, M. (2012). Focal brain lesions to
586 critical locations cause widespread disruption of the modular organization of the
587 brain. Journal of cognitive neuroscience 24, 1275-1285.
588 Grayson, D.S., Bliss-Moreau, E., Machado, C.J., Bennett, J., Shen, K., Grant, K.A., Fair,
589 D.A., and Amaral, D.G. (2016). The Rhesus Monkey Connectome Predicts
590 Disrupted Functional Networks Resulting from Pharmacogenetic Inactivation of the
591 Amygdala. Neuron 91, 453-466.
592 Guimera, R., and Nunes Amaral, L.A. (2005). Functional cartography of complex
593 metabolic networks. Nature 433, 895-900.
594 Gusnard, D.A., Raichle, M.E., and Raichle, M.E. (2001). Searching for a baseline:
595 functional imaging and the resting human brain. Nat Rev Neurosci 2, 685-694.
596 Hamilton, C., Ma, Y., and Zhang, N. (2017). Global reduction of information exchange
597 during anesthetic-induced unconsciousness. Brain structure & function 222, 3205-
598 3216.
599 Hsu, L.M., Liang, X., Gu, H., Brynildsen, J.K., Stark, J.A., Ash, J.A., Lin, C.P., Lu, H.,
600 Rapp, P.R., Stein, E.A., and Yang, Y. (2016). Constituents and functional
601 implications of the rat default mode network. Proc Natl Acad Sci U S A 113, E4541-
602 4547.

603 Humphries, M.D., and Gurney, K. (2008). Network 'small-world-ness': a quantitative
604 method for determining canonical network equivalence. PLoS One 3, e0002051.
605 Latora, V., and Marchiori, M. (2001). Efficient behavior of small-world networks. Phys Rev
606 Lett 87, 198701.
607 Lee, J.H., Durand, R., Gradinaru, V., Zhang, F., Goshen, I., Kim, D.S., Fenno, L.E.,
608 Ramakrishnan, C., and Deisseroth, K. (2010). Global and local fMRI signals driven
609 by neurons defined optogenetically by type and wiring. Nature 465, 788-792.
610 Liang, Z., King, J., and Zhang, N. (2011). Uncovering intrinsic connectional architecture
611 of functional networks in awake rat brain. J Neurosci 31, 3776-3783.
612 Liang, Z., King, J., and Zhang, N. (2012a). Anticorrelated resting-state functional
613 connectivity in awake rat brain. Neuroimage 59, 1190-1199.
614 Liang, Z., King, J., and Zhang, N. (2012b). Intrinsic organization of the anesthetized brain.
615 J Neurosci 32, 10183-10191.
616 Liang, Z., King, J., and Zhang, N. (2014). Neuroplasticity to a single-episode traumatic
617 stress revealed by resting-state fMRI in awake rats. Neuroimage 103, 485-491.
618 Liegeois, R., Li, J., Kong, R., Orban, C., Van De Ville, D., Ge, T., Sabuncu, M.R., and
619 Yeo, B.T.T. (2019). Resting brain dynamics at different timescales capture distinct
620 aspects of human behavior. Nat Commun 10, 2317.
621 Liska, A., Galbusera, A., Schwarz, A.J., and Gozzi, A. (2015). Functional connectivity
622 hubs of the mouse brain. Neuroimage 115, 281-291.
623 Liu, Y., Liang, M., Zhou, Y., He, Y., Hao, Y., Song, M., Yu, C., Liu, H., Liu, Z., and Jiang,
624 T. (2008). Disrupted small-world networks in schizophrenia. Brain 131, 945-961.
625 Lu, H., Zou, Q., Gu, H., Raichle, M.E., Stein, E.A., and Yang, Y. (2012). Rat brains also
626 have a default mode network. Proc Natl Acad Sci U S A 109, 3979-3984.
627 Ma, Y., Hamilton, C., and Zhang, N. (2017). Dynamic Connectivity Patterns in Conscious
628 and Unconscious Brain. Brain connectivity 7, 1-12.
629 Ma, Z., Perez, P., Ma, Z., Liu, Y., Hamilton, C., Liang, Z., and Zhang, N. (2018). Functional
630 atlas of the awake rat brain: A neuroimaging study of rat brain specialization and
631 integration. Neuroimage 170, 95-112.
632 Ma, Z., and Zhang, N. (2018). Temporal transitions of spontaneous brain activity. eLife 7.
633 Nair, J., Klaassen, A.L., Arato, J., Vyssotski, A.L., Harvey, M., and Rainer, G. (2018).
634 Basal forebrain contributes to default mode network regulation. Proc Natl Acad Sci
635 U S A 115, 1352-1357.
636 Newman, M.E. (2002). Assortative mixing in networks. Phys Rev Lett 89, 208701.
637 Newman, M.E. (2004). Fast algorithm for detecting community structure in networks.
638 Phys Rev E Stat Nonlin Soft Matter Phys 69, 066133.
639 Newman, M.E. (2006). Modularity and community structure in networks. Proc Natl Acad
640 Sci U S A 103, 8577-8582.
641 Raichle, M.E., MacLeod, A.M., Snyder, A.Z., Powers, W.J., Gusnard, D.A., and Shulman,
642 G.L. (2001). A default mode of brain function. Proc Natl Acad Sci U S A 98, 676-
643 682.
644 Rorden, C., and Karnath, H.O. (2004). Using human brain lesions to infer function: a relic
645 from a past era in the fMRI age? Nat Rev Neurosci 5, 813-819.
646 Rubinov, M., and Sporns, O. (2010). Complex network measures of brain connectivity:
647 uses and interpretations. Neuroimage 52, 1059-1069.

Seeley, W.W., Crawford, R.K., Zhou, J., Miller, B.L., and Greicius, M.D. (2009). Neurodegenerative diseases target large-scale human brain networks. Neuron 62, 42-52.

Stafford, J.M., Jarrett, B.R., Miranda-Dominguez, O., Mills, B.D., Cain, N., Mihalas, S., Lahvis, G.P., Lattal, K.M., Mitchell, S.H., David, S.V.*, et al.* (2014). Large-scale topology and the default mode network in the mouse connectome. Proc Natl Acad Sci U S A 111, 18745-18750.

Swanson, L.W. (2004). Brain Maps: Structure of the Rat Brain. (Elsevier).

van den Heuvel, M.P., Scholtens, L.H., and de Reus, M.A. (2016). Topological organization of connectivity strength in the rat connectome. Brain structure & function 221, 1719-1736.

van den Heuvel, M.P., and Sporns, O. (2013). Network hubs in the human brain. Trends Cogn Sci 17, 683-696.

Vincent, J.L., Patel, G.H., Fox, M.D., Snyder, A.Z., Baker, J.T., Van Essen, D.C., Zempel, J.M., Snyder, L.H., Corbetta, M., and Raichle, M.E. (2007). Intrinsic functional architecture in the anaesthetized monkey brain. Nature 447, 83-86.

Wang, J., Zuo, X., and He, Y. (2010). Graph-based network analysis of resting-state functional MRI. Front Syst Neurosci 4, 16.

Warren, D.E., Power, J.D., Bruss, J., Denburg, N.L., Waldron, E.J., Sun, H., Petersen, S.E., and Tranel, D. (2014). Network measures predict neuropsychological outcome after brain injury. Proc Natl Acad Sci U S A 111, 14247-14252.

Whissell, P.D., Tohyama, S., and Martin, L.J. (2016). The Use of DREADDs to Deconstruct Behavior. Front Genet 7, 70.

Whitfield-Gabrieli, S., and Ford, J.M. (2012). Default mode network activity and connectivity in psychopathology. Annu Rev Clin Psychol 8, 49-76.

Yoshida, K., Mimura, Y., Ishihara, R., Nishida, H., Komaki, Y., Minakuchi, T., Tsurugizawa, T., Mimura, M., Okano, H., Tanaka, K.F., and Takata, N. (2016). Physiological effects of a habituation procedure for functional MRI in awake mice using a cryogenic radiofrequency probe. J Neurosci Methods 274, 38-48.

Yuan, B., Fang, Y., Han, Z., Song, L., He, Y., and Bi, Y. (2017). Brain hubs in lesion models: Predicting functional network topology with lesion patterns in patients. Sci Rep 7, 17908.

Zhang, D., and Raichle, M.E. (2010). Disease and the brain's dark energy. Nat Rev Neurol 6, 15-28.

Zhang, N., Rane, P., Huang, W., Liang, Z., Kennedy, D., Frazier, J.A., and King, J. (2010). Mapping resting-state brain networks in conscious animals. J Neurosci Methods 189, 186-196.

Zhou, Z.C., Salzwedel, A.P., Radtke-Schuller, S., Li, Y., Sellers, K.K., Gilmore, J.H., Shih, Y.Y., Frohlich, F., and Gao, W. (2016). Resting state network topology of the ferret brain. Neuroimage 143, 70-81.

Zou, Q.H., Zhu, C.Z., Yang, Y., Zuo, X.N., Long, X.Y., Cao, Q.J., Wang, Y.F., and Zang, Y.F. (2008). An improved approach to detection of amplitude of low-frequency fluctuation (ALFF) for resting-state fMRI: fractional ALFF. J Neurosci Methods 172, 137-141.

693 **Figure Captions.**

694 **Figure 1**. *Schematic diagram of the experimental paradigm.*

695 **Figure 2**. *Validation of the inhibitory effect of DREADDs*. **A**) Visual stimulation paradigm;
696 Examples of spiking activity in the SC in response to **B**) 1 flash (100ms/flash) and **C**) 5
697 flashes (100ms/flash) of light stimulation after saline and CNO injections; **D**) DREADD
698 suppressed evoked firing rate ($p < 0.005$ for both 1 flash and 5 flash stimuli, 15 trials per
699 animal, per condition, n=3); **E**) DREADD suppressed spontaneous firing rates during 5s
700 before visual stimulation ($p < 0.005$); **F**) Averaged spectrograms after saline (left) and
701 CNO (right) injections; **G**) Chemogenetic inhibition reduced local field potential power (3-
702 300Hz) in the SC. ***: $p < 0.005$.

703 **Figure 3.** *Suppressing dACC reduced its spontaneous BOLD signal, RSFC, and local*
704 *network structure.* **A**) Amplitude of spontaneous BOLD activity in the DREADD (19
705 animals, 78 scans) and sham groups (8 animals, 41scans); **B**) Averaged seedmaps after
706 saline and CNO injections (one-sample t-test, linear mixed model, $p < 0.0005$, FDR
707 corrected); **C**) Left: averaged RSFC matrices after saline and CNO injections in the
708 DREADD group. Right: connections exhibiting significant RSFC change (two-sample t-
709 test, linear mixed model, $p < 0.05$, FDR corrected). **D**) These connections were grouped
710 into multiple brain systems. Line thickness represents the total number of connections
711 with significant RSFC changes between the two systems; **E**) The size of the dACC-
712 associated community structure as a function of graph density in the DREADD group after
713 saline and CNO injections (two-sample t-test, linear mixed model). *: $p < 0.05$; **: $p < 0.01$.

714 **Figure 4.** *Suppressing dACC disrupted activity across the DMN.* A) DMN constructed
715 using fractional amplitude of low-frequency fluctuations (fALFF) after saline and CNO
716 injections; B) Voxel-wise fALFF changes after DREADD inhibition ($p < 0.05$, linear mixed
717 model, family-wise error corrected); C) RSFC between DMN regions in the DREADD and
718 sham groups after saline and CNO injections, respectively; D) RSFC changes within the
719 DMN after dACC inhibition ($p < 0.05$, linear mixed model, FDR corrected); E) Negative
720 and positive RSFC changes after dACC inhibition ($p < 0.05$, linear mixed model, FDR
721 corrected).

722 **Figure 5**. *Suppressing dACC changed DMN-related behavior (n=10).* **A**) Total distance
723 traveled in homecage (45 min); **B**) Mean speed; **C**) Total mobile time; **D**) Total immobile
724 time for at least 2s. **E**) Total rearing behavior. *: $p < 0.05$; ***: $p < 0.005$.

725 **Figure 6**. *Suppressing a hub node changed whole-brain network topology.* **A**) Network
726 resilience; **B**) Small-worldness; **C**) Network segregation; **D**) Network integration. Linear
727 mixed model; DREADD: n = 19, 78 scans; sham: n = 8, 41 scans. *: $p < 0.05$; **: $p < 0.01$.

728 **Figure 7**. *New hub emerged after the inactivation of an old hub*. **A**) Hub scores without
729 and with dACC inactivation, respectively; **B**) The degree of dACC and ventral RSC
730 without and with dACC inactivation (linear mixed model; n = 19, 78 scans). *: $p < 0.05$; **:
731 $p < 0.01$; ***: $p < 0.005$.

732 **Figure 8.** *Suppressing a non-hub node did not change whole-brain network topology.* A)
733 Amplitude of spontaneous BOLD activity in the primary visual cortex after CNO and saline
734 injections ($p < 0.05$, n=8, 66 scans); B) Network resilience; C) Small-worldness; D)
735 Network segregation; E) Network integration.

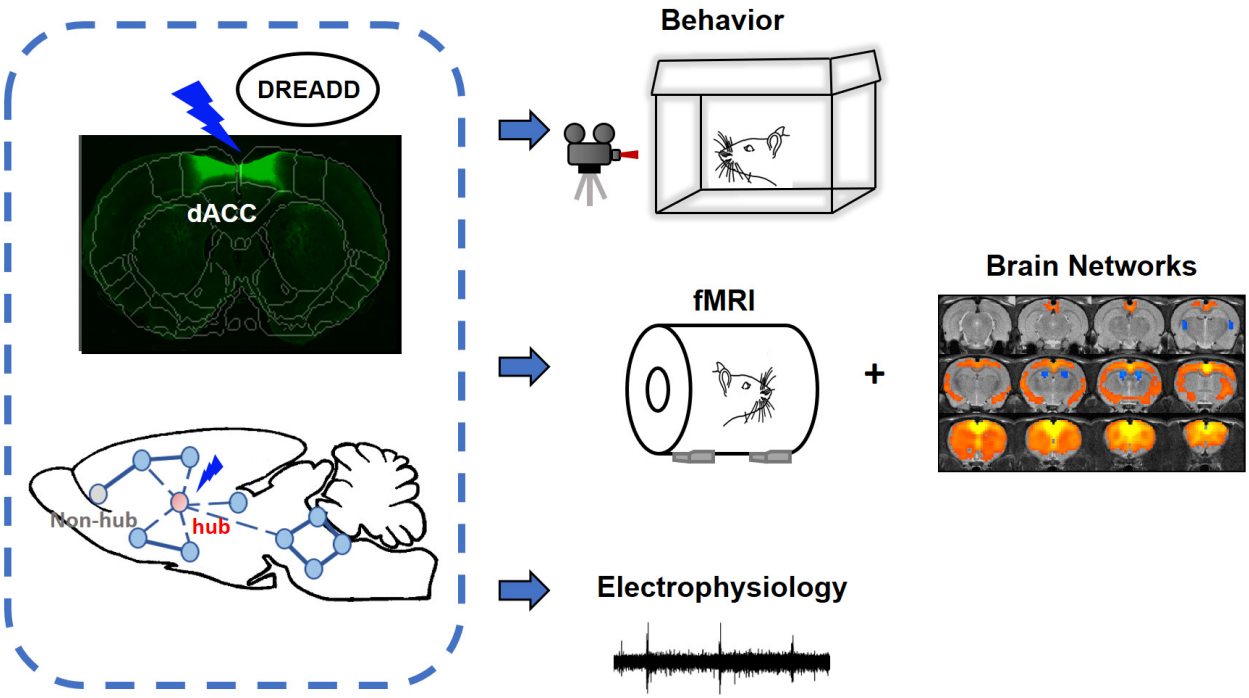

Figure 1. *Schematic diagram of the experimental paradigm.*

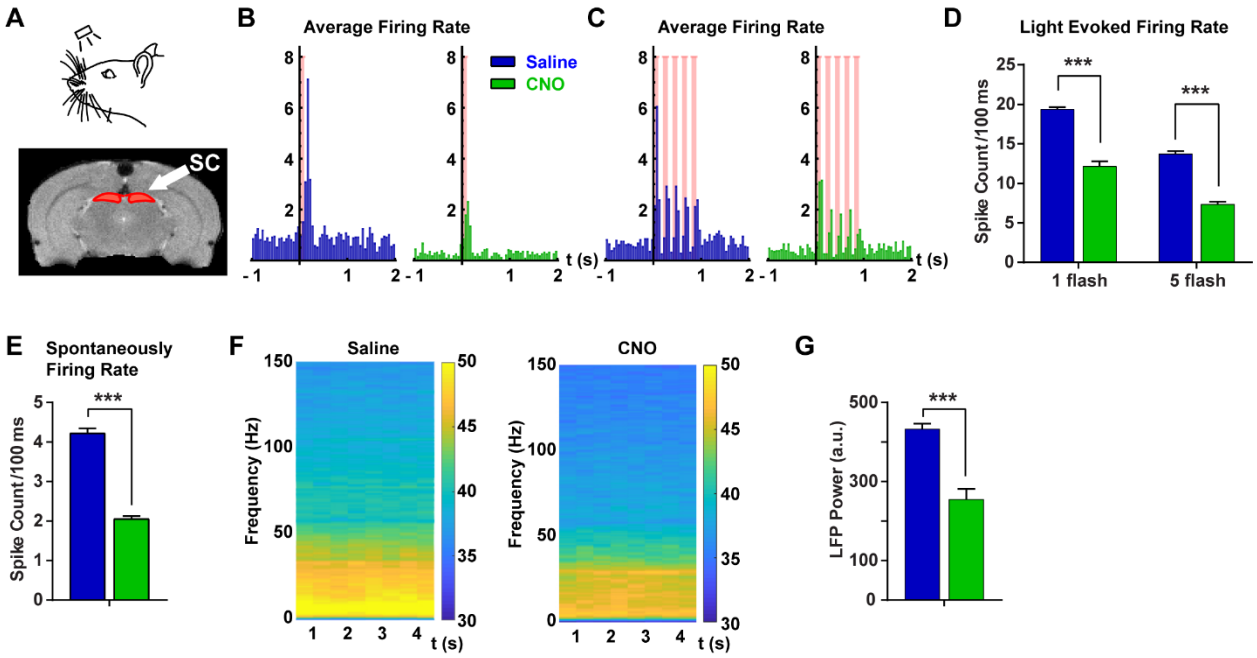

Figure 2. *Validation of the inhibitory effect of DREADDs*. **A**) Visual stimulation paradigm; Examples of spiking activity in the SC in response to **B**) 1 flash (100ms/flash) and **C**) 5 flashes (100ms/flash) of light stimulation after saline and CNO injections; **D**) DREADD suppressed evoked firing rate ($p < 0.005$ for both 1 flash and 5 flash stimuli, 15 trials per animal, per condition, n=3); **E**) DREADD suppressed spontaneous firing rates during 5s before visual stimulation ($p < 0.005$); **F**) Averaged spectrograms after saline (left) and CNO (right) injections; **G**) Chemogenetic inhibition reduced local field potential power (3-300Hz) in the SC. ***: $p < 0.005$.

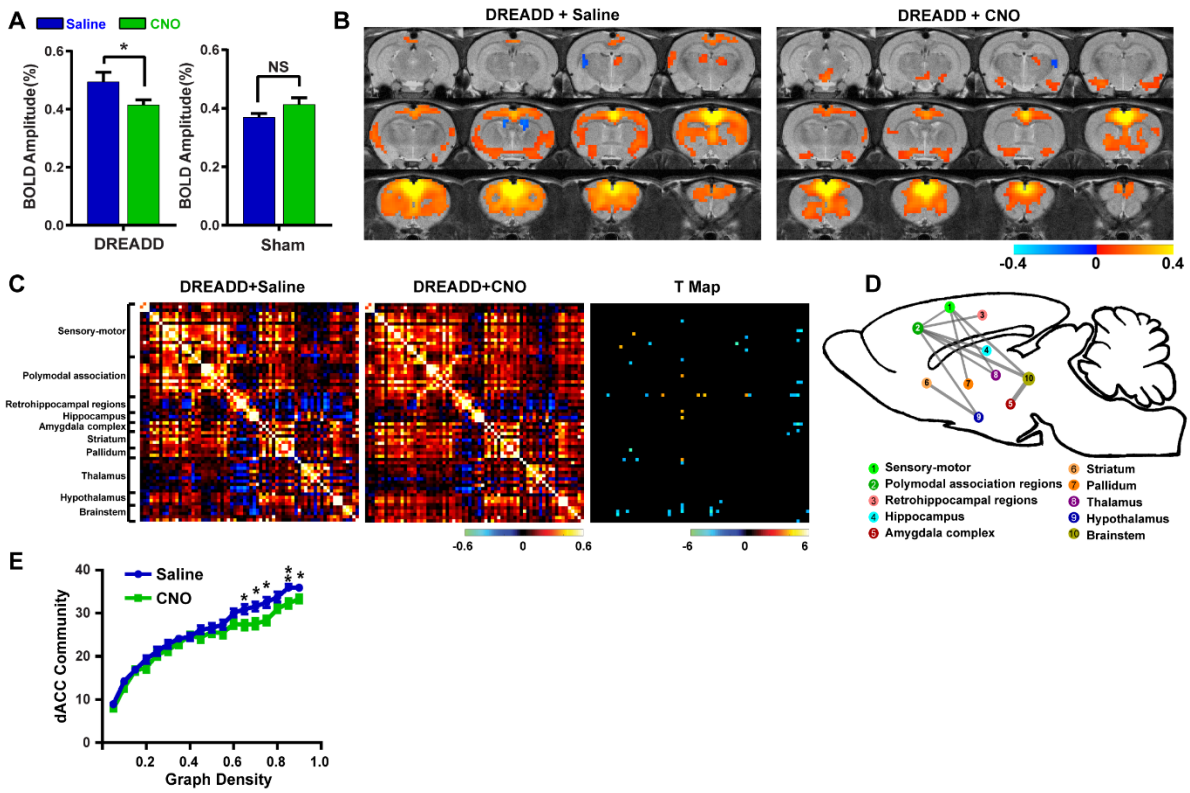

Figure 3. *Suppressing dACC reduced its spontaneous BOLD signal, RSFC, and local network structure.* **A**) Amplitude of spontaneous BOLD activity in the DREADD (19 animals, 78 scans) and sham groups (8 animals, 41scans); **B**) Averaged seedmaps after saline and CNO injections (one-sample t-test, linear mixed model, $p < 0.0005$, FDR corrected); **C**) Left: averaged RSFC matrices after saline and CNO injections in the DREADD group. Right: connections exhibiting significant RSFC change (two-sample t-test, linear mixed model, $p < 0.05$, FDR corrected). **D**) These connections were grouped into multiple brain systems. Line thickness represents the total number of connections with significant RSFC changes between the two systems; **E**) The size of the dACC-associated community structure as a function of graph density in the DREADD group after saline and CNO injections (two-sample t-test, linear mixed model). *: $p < 0.05$; **: $p < 0.01$.

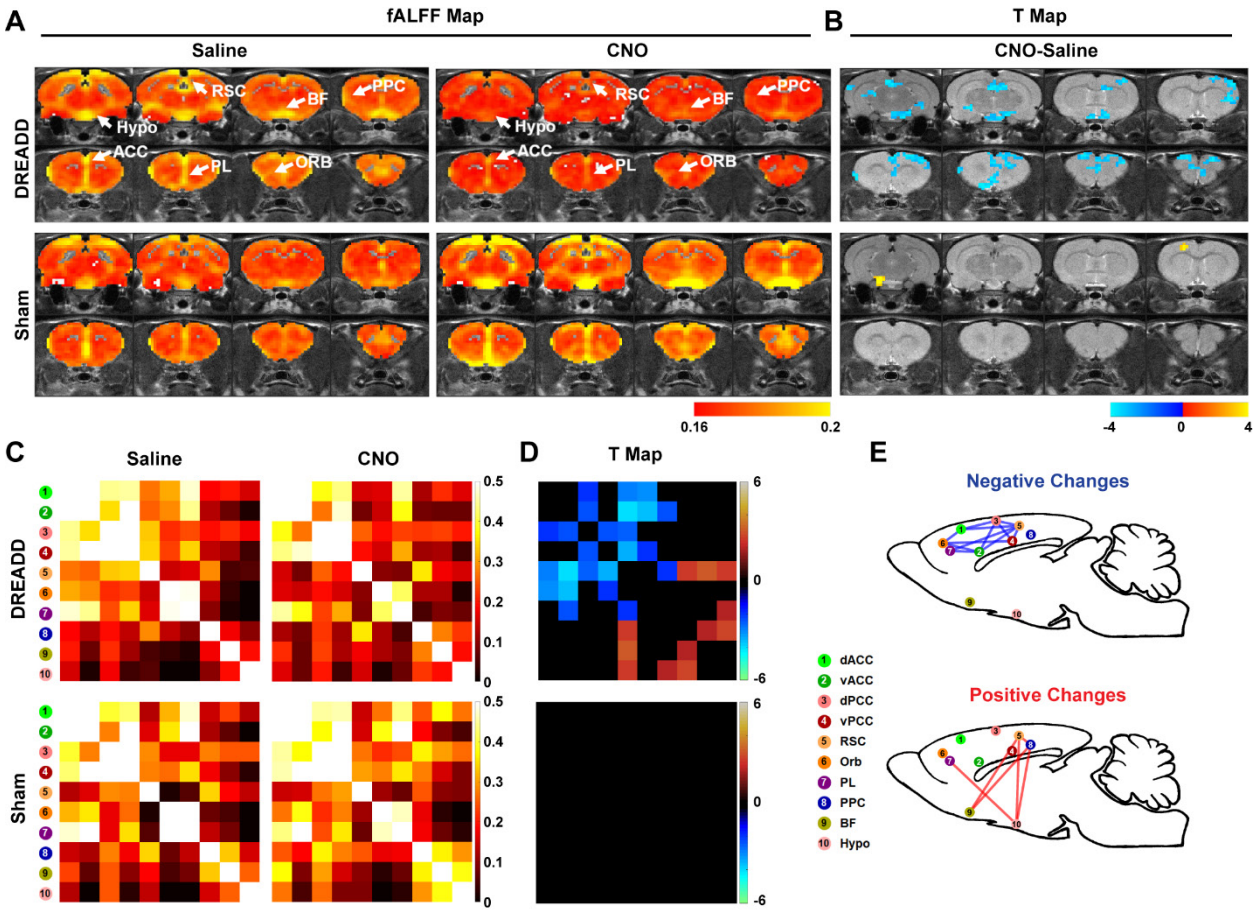

Figure 4. *Suppressing dACC disrupted activity across the DMN.* **A**) DMN constructed using fractional amplitude of low-frequency fluctuations (fALFF) after saline and CNO injections; **B**) Voxel-wise fALFF changes after DREADD inhibition ($p < 0.05$, linear mixed model, family-wise error corrected); **C**) RSFC between DMN regions in the DREADD and sham groups after saline and CNO injections, respectively; **D**) RSFC changes within the DMN after dACC inhibition ($p < 0.05$, linear mixed model, FDR corrected); **E**) Negative and positive RSFC changes after dACC inhibition ($p < 0.05$, linear mixed model, FDR corrected).

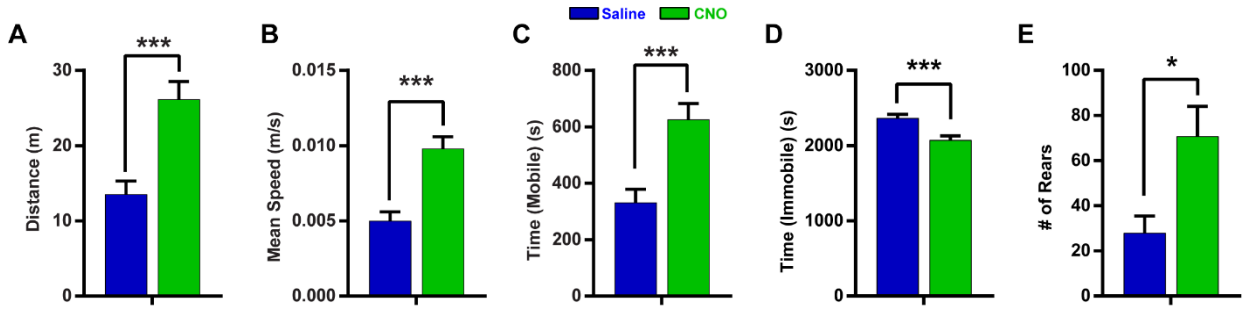

Figure 5. *Suppressing dACC changed DMN-related behavior (n=10).* **A**) Total distance traveled in homecage (45 min); **B**) Mean speed; **C**) Total mobile time; **D**) Total immobile time for at least 2s. **E**) Total rearing behavior. *: $p < 0.05$; ***: $p < 0.005$.

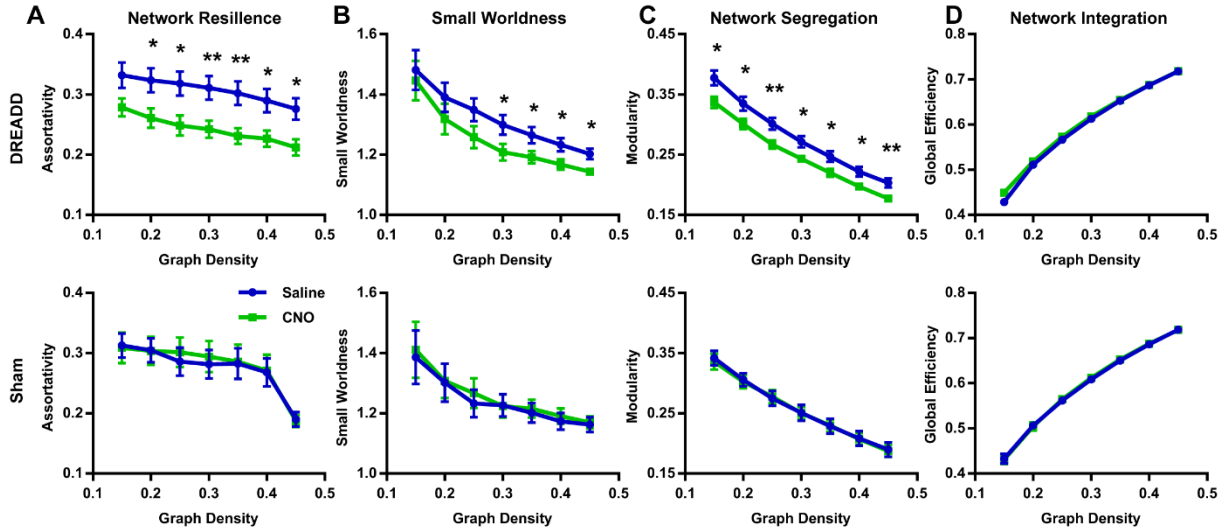

Figure 6. *Suppressing a hub node changed whole-brain network topology.* **A**) Network resilience; **B**) Small-worldness; **C**) Network segregation; **D**) Network integration. Linear mixed model; DREADD: n = 19, 78 scans; sham: n = 8, 41 scans. *: $p < 0.05$; **: $p < 0.01$.

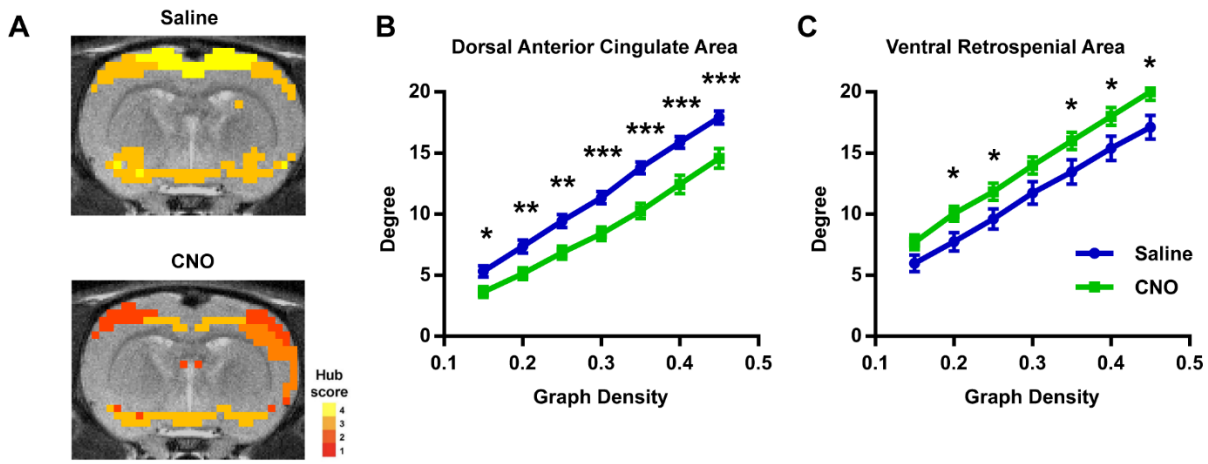

Figure 7. *New hub emerged after the inactivation of an old hub*. **A**) Hub scores without and with dACC inactivation, respectively; **B**) The degree of dACC and ventral RSC without and with dACC inactivation (linear mixed model; n = 19, 78 scans). *: $p < 0.05$; **: $p < 0.01$; ***: $p < 0.005$.

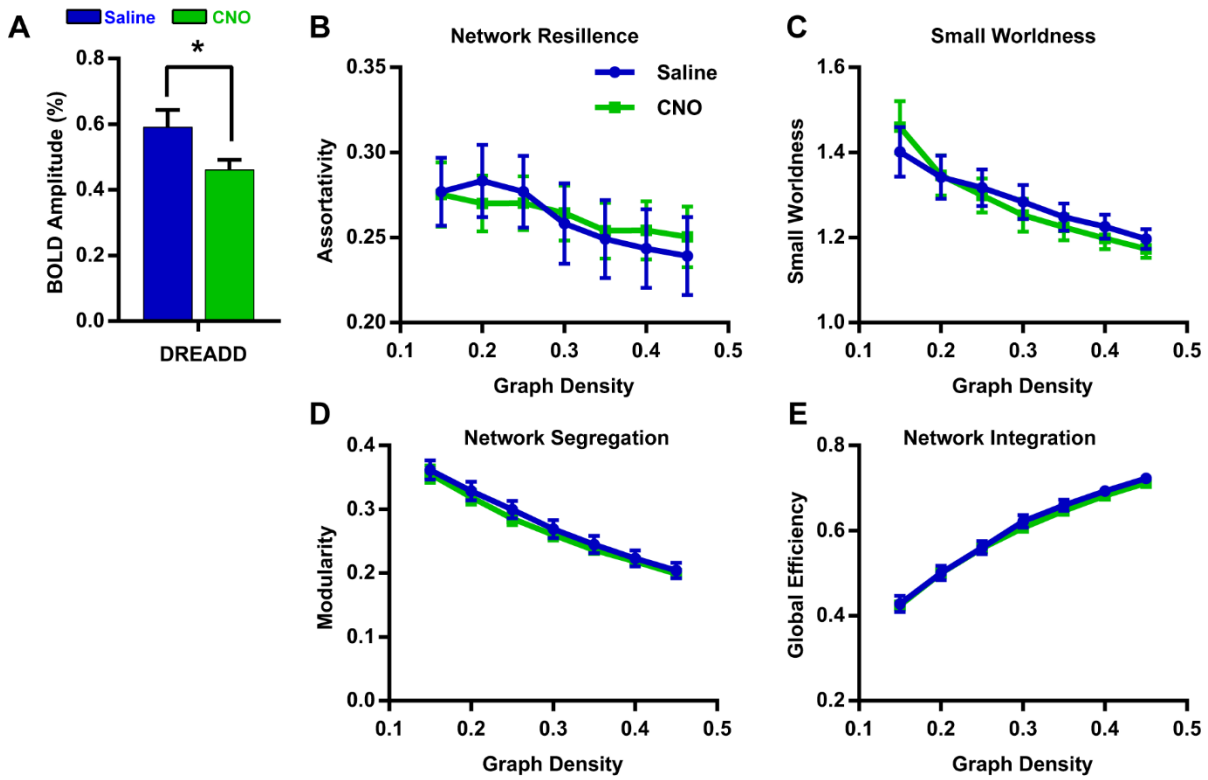

Figure 8. *Suppressing a non-hub node did not change whole-brain network topology.* **A**) Amplitude of spontaneous BOLD activity in the primary visual cortex after CNO and saline injections ($p < 0.05$, n=8, 66 scans); **B**) Network resilience; **C**) Small-worldness; **D**) Network segregation; **E**) Network integration.

How brain reacts to attack at a local region

Wenyu Tu[1], Zilu Ma[2], Yuncong Ma[2] and Nanyin Zhang[1,2]*

[1] Neuroscience Program, The Huck Institutes of the Life Sciences, The Pennsylvania State University, University Park, PA 16802, USA

[2] Department of Biomedical Engineering, The Pennsylvania State University, University Park, PA 16802, USA

***Address for correspondence:**

Nanyin Zhang, PhD

Professor of Biomedical Engineering and Electrical Engineering

Lloyd & Dorothy Foehr Huck Chair in Brain Imaging

The Huck Institutes of the Life Sciences

The Pennsylvania State University

W-341 Millennium Science Complex, University Park, PA 16802, USA

Email: nuz2@psu.edu

Supplementary Information

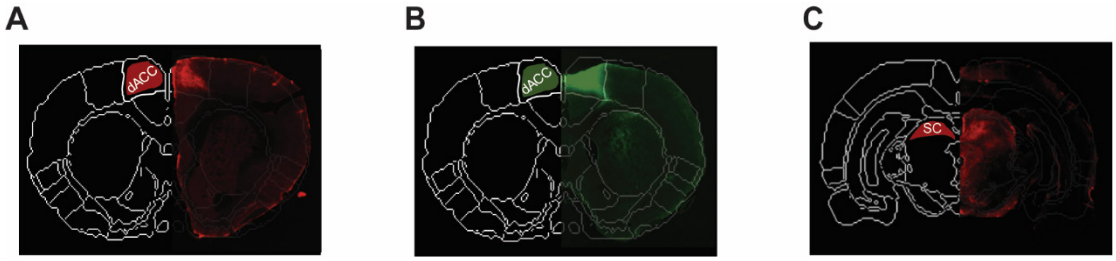

Figure S1. *Representative Histology.* **A**) DREADD dACC; **B**) Sham dACC; **C**) DREADD Superior colliculus. Anatomical definition of the regions are shown in the left hemisphere.

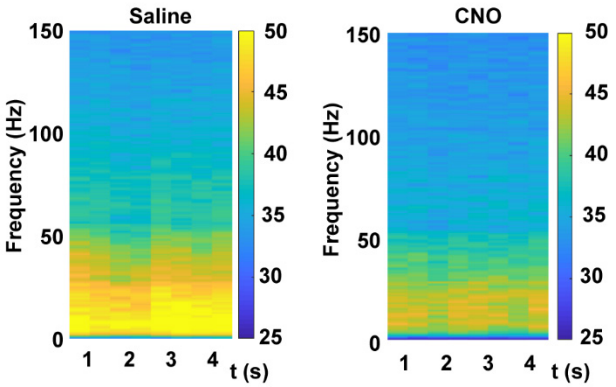

Figure S2. *LFP spectrograms after saline and CNO injections in a representative rat with DREADDs infused in the SC*.

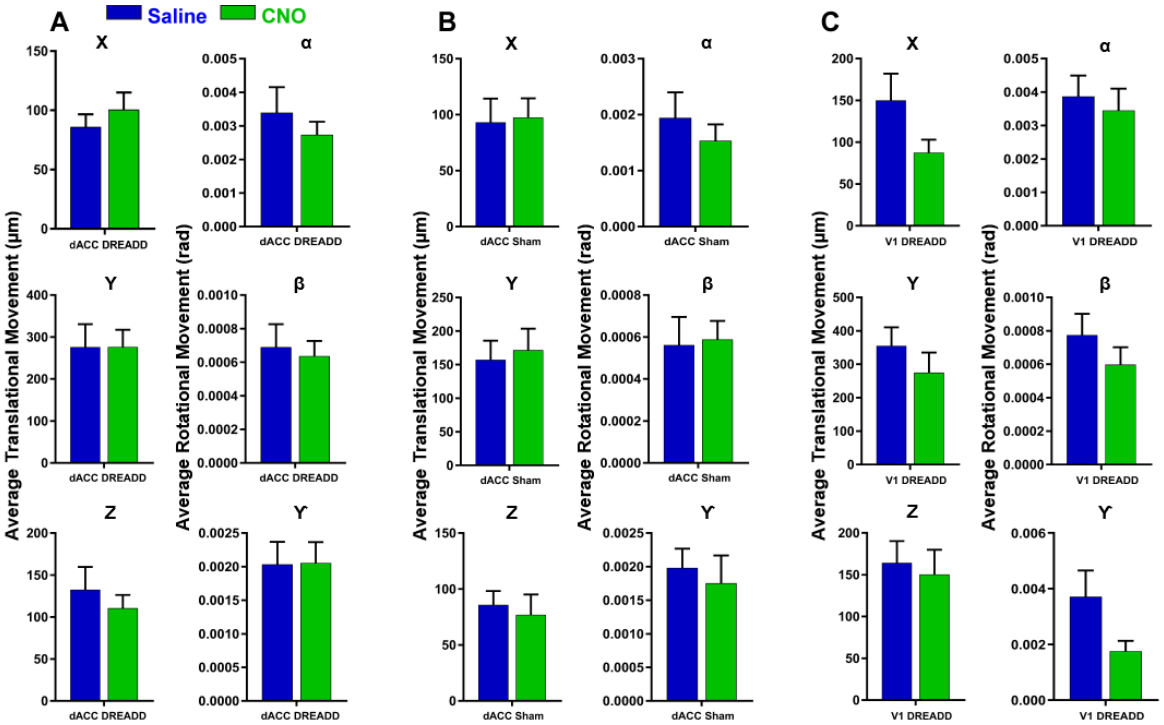

Figure S3. *Motion levels in all groups.* **A**. dACC DREADD (n=19, 78 scans); **B**. dACC sham (n=8, 41 scans); **C**. V1 DREADD (n=8, 66 scans). Left column: translational movement (in µm). Right column: rotational movement (in rad) (linear mixed model, $p > 0.05$ for all 6 parameters in all groups).

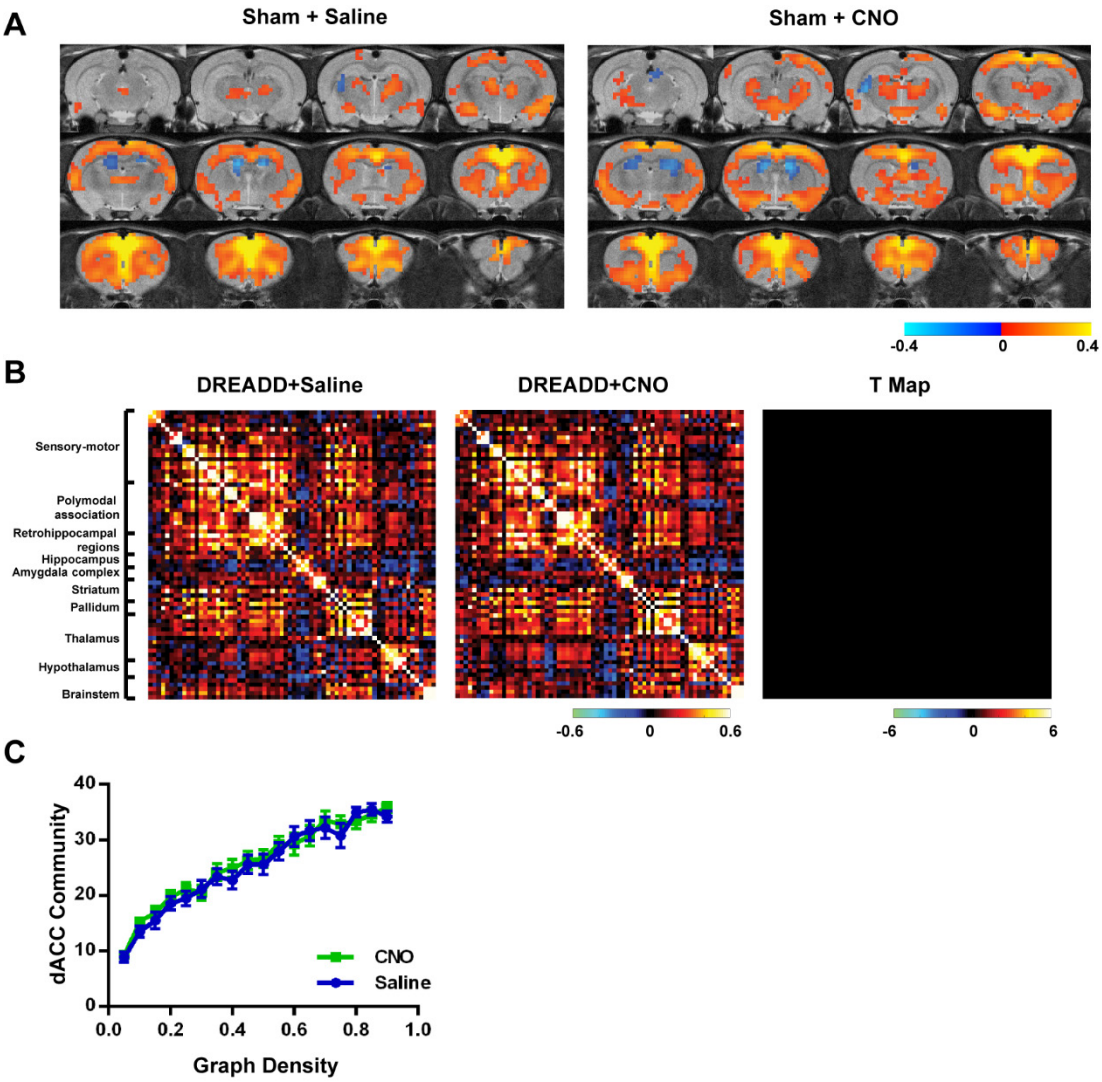

Figure S4. *Sham group did not show reduced RSFC or dACC community size.* **A**) Averaged seedmaps after CNO and saline injections in the sham group (one sample t test, linear mixed model, p<0.0005, FDR corrected; n=8, 41scans); **B**) Averaged ROI-wise RSFC matrices after saline and CNO injections in the sham group. No connections exhibit RSFC changes (two-sample t-tests, linear mixed model, p < 0.05, FDR corrected, n=8, 41scans). **C**) The size of the dACC-associated community as a function graph density after saline and CNO injections in the sham group (two-sample t-tests, linear mixed model, p > 0.05 for all densities tested, n=8, 41 scans).

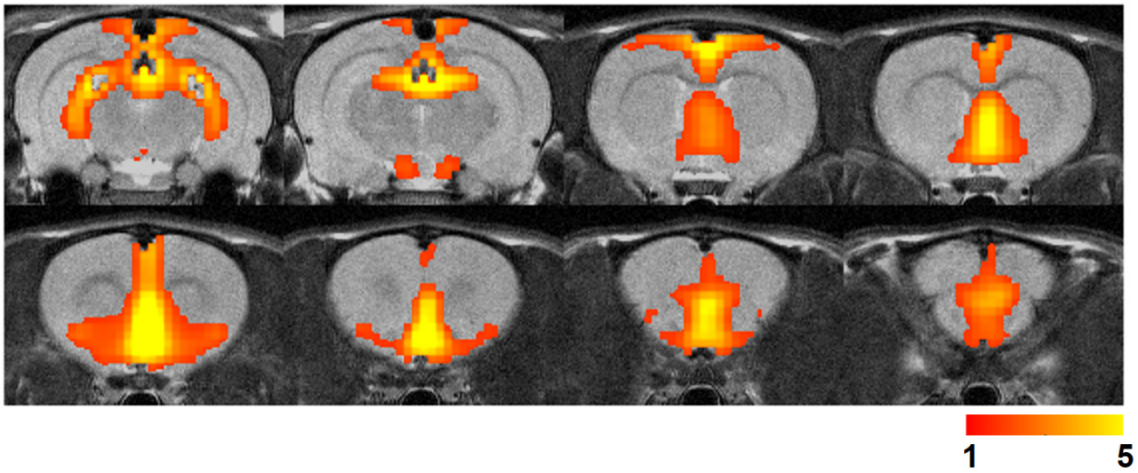

Figure S5. *DMN pattern revealed by independent component analysis.*

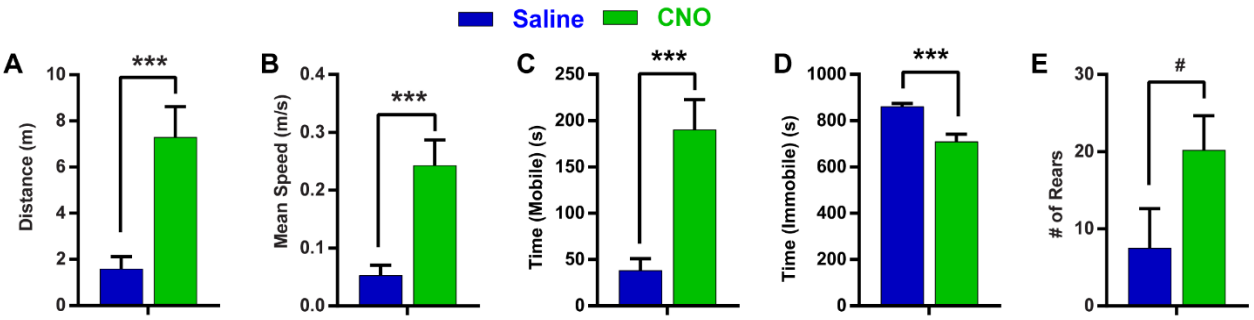

Figure S6. *Suppressing dACC changed DMN-related behavior.* **A**) Total distance traveled; **B**) Mean speed; **C**) Total mobile time; **D**) Total time when animal was immobile for at least 2s; **E**) total number of rears in home-cage in the last 15 min of tests (i.e. 30 min after injection of CNO or Saline). n=10; #: p = 0.07.

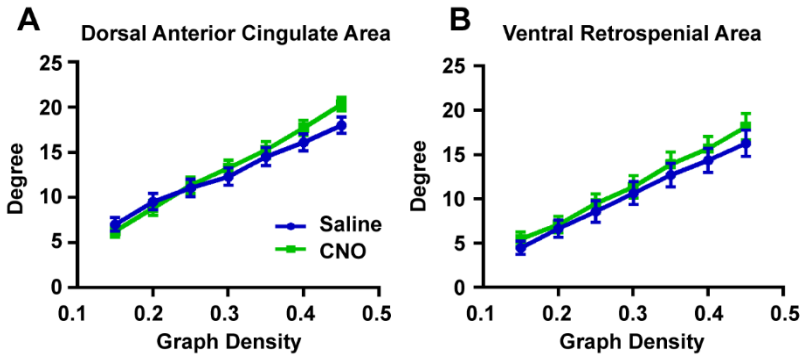

Figure S7. *Sham group did not show changed degree of the dACC or RSC.* Degree changes of the dorsal anterior cingulate area and ventral retrosplenial area in the dACC sham group (two-sample t-tests, linear mixed model, $p > 0.05$ for all densities tested, n=8, 41 scans).

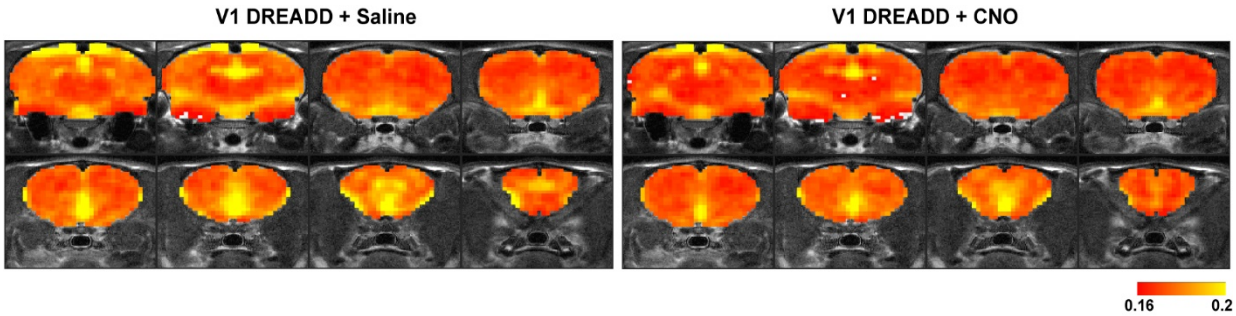

Figure S8. *Suppressing V1 did not affect DMN activity*. DMN constructed using fALFF in the V1 DREADD group after saline and CNO injections (n=8, 66 scans).

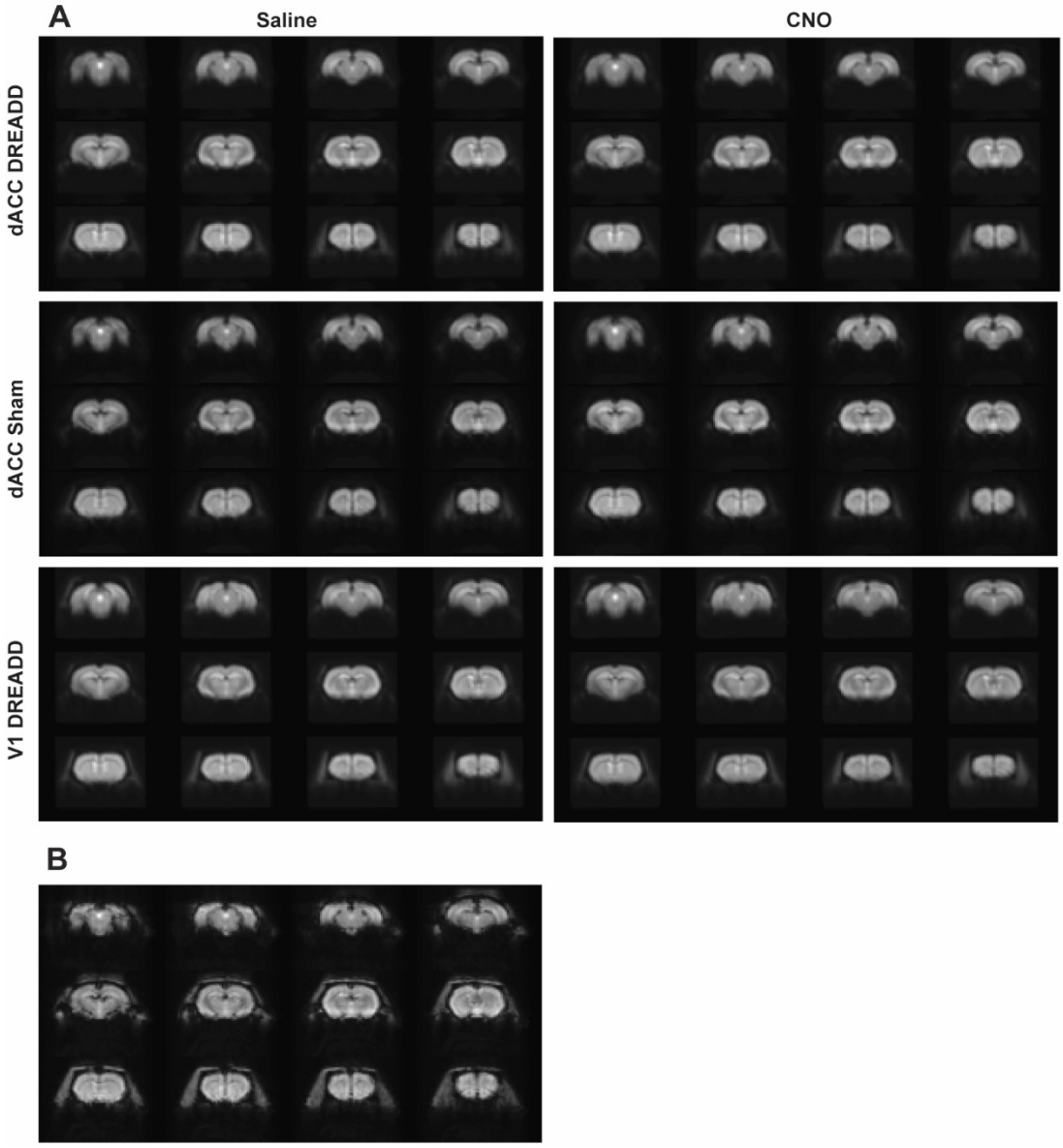

Figure S9. *Raw EPI data.* A. Averaged EPI image for each group and condition (dACC DREADD: n=19, 78 scans; dACC Sham: n=8, 41 scans; V1 DREADD: n=8, 66 scans); B. Example of a single EPI volume.